

BLACK HOLE FUELING IN GALAXY MERGERS: A HIGH-RESOLUTION ANALYSIS

JOAQUIN PRIETO¹, ANDRÉS ESCALA¹, GEORGE C. PRIVON² & JUAN D'ETIGNY¹

¹Departamento de Astronomía, Universidad de Chile, Casilla 36-D, Santiago, Chile.

²Department of Astronomy, University of Florida, 211 Bryant Space Sciences Center, Gainesville, FL 32611, USA.

Draft version January 26, 2021

ABSTRACT

Using parsec scale resolution hydrodynamical adaptive mesh refinement simulations we have studied the mass transport process throughout a galactic merger. The aim of such study is to connect both the peaks of mass accretion rate onto the BHs and star formation bursts with both gravitational and hydrodynamic torques acting on the galactic gaseous component. Our merger initial conditions were chosen to mimic a realistic system. The simulations include gas cooling, star formation, supernovae feedback, and AGN feedback. Gravitational and hydrodynamic torques near pericenter passes trigger gas funneling to the nuclei which is associated with bursts of star formation and black hole growth. Such episodes are intimately related with both kinds of torques acting on the galactic gas. Pericenters trigger both star formation and mass accretion rates of \sim few $(1 - 10) M_{\odot}/\text{yr}$. Such episodes last $\sim (50 - 75)$ Myrs. Close passes also can produce black hole accretion that approaches and reaches the Eddington rate, lasting \sim few Myrs. Our simulation shows that both gravitational and hydrodynamic torques are enhanced at pericenter passes with gravitational torques tending to have higher values than the hydrodynamic torques throughout the merger. We also find that in the closest encounters, hydrodynamic and gravitational torques can be comparable in their effect on the gas, the two helping in the redistribution of both angular momentum and mass in the galactic disc. Such phenomena allow inward mass transport onto the BH influence radius, fueling the compact object and lighting up the galactic nuclei.

Subject headings: galaxies: formation — large-scale structure of the universe — stars: formation — turbulence.

1. INTRODUCTION

Cosmological N-body numerical simulations of structure formation shows that dark matter (DM) haloes were formed by mergers between smaller haloes in a hierarchical way (e.g. Angulo et al. 2012). Similar kinds of simulations including baryonic physics have shown that galaxies were formed inside DM haloes in this hierarchical model (e.g. Dubois et al. 2014; Genel et al. 2014). In this sense, mergers and interaction between galaxies are a fundamental piece of the galaxy formation process and certainly they influence the galaxies evolution. In fact, observation of irregular and disrupted systems are consistent with mergers and interactions between galaxies (e.g. Toomre & Toomre 1972; Schweizer 1982; Engel et al. 2010; Bussmann et al. 2012).

The infrared and optical properties of interacting galaxies are different compared with isolated systems (e.g. Sanders & Mirabel 1996). Such differences can be a consequence of star formation burst associated to galactic interactions (e.g. Sanders et al. 1998; Duc et al. 1997; Jogee et al. 2009). Beside the radiative signatures of star formation, some interacting galaxies also show nuclear activity which can be associated with black hole (BH) fueling (e.g. Petric 2011; Stierwalt et al. 2013). These two features, i.e. SF bursts and active galactic nuclei (AGN), suggest that galactic encounters are able to redistribute gas inside galaxies, moving material toward their central regions to feed massive BHs and trigger SF bursts (e.g. Barnes & Hernquist 1991; Mihos & Hernquist 1996; Springel et al. 2005).

Smoothed Particle Hydrodynamic (SPH) numerical simulations of galactic mergers with \sim few $(10 - 100)$

pc of resolution have shown that gravitational torques are able to produce inflows of gas toward the galactic central regions (e.g. Barnes & Hernquist 1991; Wurster & Thacker 2013; Newton & Kay 2013; Blumenthal & Barnes 2018). Such inflows, increase the gas density of galactic centers enhancing SF (e.g. Teyssier 2010; Powell et al. 2013) and at the same time are able to feed central super massive BHs triggering AGN activity (e.g. Sanders et al. 1998; Bahcall et al. 1995; Debuhr et al. 2011). Besides the low resolution SPH simulations including both SNe and AGN feedback mentioned above (e.g. Debuhr et al. 2011; Wurster & Thacker 2013; Newton & Kay 2013), using an adaptive mesh refinement (AMR) simulation of ~ 8 pc of resolution Gabor et al. (2016) have also shown that pericenter passes correlate with peaks in both BH and stellar activity but did not analyze the source of torques. The lack of parsec scale resolution AMR simulations studying mass transport in galaxy mergers strengthen the relevance of torque analysis in this kind of experiments. However studies of mass transport in \sim pc-resolution simulations have not been performed.

When choosing to deal with idealized mergers using AMR codes over a Lagrangian code, problems with the advection of material and grid alignment issues may arise, which could result in a loss of angular momentum conservation (Wadsley et al. 2008; Hahn et al. 2010; Hopkins 2015). This issues are minimized as high spatial resolution is imposed at central galaxy regions, minimizing spurious field misalignments, and also, since pericenter passes have short durations (few orbital times at most) there are no significant orbital angular momentum

deviations with respect to the ideal case. Furthermore, the galaxies are maintained at resolutions that are high enough for the AMR technique to be effective at resolving shocks throughout the merger process and therefore contact discontinuities are captured.

As the objective of our simulation is to properly and fully characterize a generic galaxy merger that exhibits realistic dynamics, we have to choose appropriate orbital initial conditions that have been proven capable of nearly-reproducing such observed controlled environments. Due to the degeneracy of the problem and the large parameter space of galaxy interactions, constraining the initial conditions with hydrodynamic simulations would be prohibitively time-consuming. Privon et al. (2013) used the Identikit code to find the orbital parameters capable to reproduce the morphology and kinematics of tidal features of four known observed galaxy mergers (NGC 5257/8, The Mice, Antennae and NGC 2623). In this work we will adopt their orbital parameters (as an ansatz) for NGC 2623. Whilst the objective of this work will not be to reproduce neither the morphology of this system, we cite its characteristics as order of magnitude control values.

NGC 2623 is a low-redshift, luminous infrared galaxy (LIRG) with an infrared luminosity of $L_{\text{IR}} = 3.6 \times 10^{11} L_{\odot}$ from Armus et al. (2009). The system has been classified as an M4 merger (Larson et al. 2016), i.e. they are galaxies with apparent single nucleus and evident tidal tails. The merger shows two tidal tails of $\sim 20 - 25$ kpc in length, approximately with a single nucleus in IR (e.g. Evans et al. 2008). Sanders & Mirabel (1996) found a system stellar mass of $M_{\star} = 2.95 \times 10^{10} M_{\odot}$ with a molecular hydrogen mass of $M_{\text{H}_2} = 6.76 \times 10^9 M_{\odot}$. This values do not stray afar from typical LIRG values found in samples like the GOALS survey (Armus et al. 2009). Haan et al. (2011) show that although there is some spread in the central BH mass values found in the GOALS survey, masses are generally found in the $10^7 - 10^9 M_{\odot}$ range.

In this paper, for the first time we will study the evolution of a merger system from its early stages, up to the point where their BHs coalesce, using a ~ 3 pc resolution AMR simulation including SF, supernovae (SNe) feedback, BH particles and AGN feedback. The goal of this paper is to understand the connection between torques, SF bursts and AGN activity in such large scale galactic environments with unprecedented high resolution, resolving the BH influence radius.

The paper is organized as follows. In §2 we describe the numerical details of the experiment, in §3 we show our results and in §4 we present our discussion and conclusions.

2. METHODOLOGY AND NUMERICAL SIMULATION DETAILS

2.1. Initial conditions

As already mentioned, in this work we use the parameters found in Privon et al. (2013) for NGC 2623, as initial conditions for a high resolution hydrodynamic numerical simulation. Table 2.1 shows the initial orbital parameters of the simulated merger used in this work and table 2.1 shows the initial position and velocity for both galactic centers.

In addition to the orbital ICs, it is necessary to specify both the mass content and the mass distribution for each component of the galaxies, including the gaseous disc, stellar disc, and stellar bulge. In order to create ICs for the DM haloes, gas and stars for each galaxy we have used the DICE code (Perret et al. 2014). For our setup the gaseous disc follows an exponential profile with a characteristic radius of 1 kpc. The stellar disc is modelled with a Myamoto-Nagai profile with a characteristic radius of 0.677 kpc. The stellar bulge follows a Einasto profile with a characteristic radius of 0.6 kpc. Finally for the DM profile we employ a Navarro Frenk and White profile (Navarro, Frenk & White 1996) with a concentration parameter equal to 10. The SFR in the stellar disc follows Bouché (2010). Table 2.1 shows a complete summary of the galactic parameters of the system.

TABLE 1
INITIAL ORBITAL PARAMETERS.

D_{ini} [kpc]	e	p [kpc]	μ	$(i_1; \omega_1)$	$(i_2; \omega_2)$
50.0	1.0	0.6	1.0	(30°; 330°)	(25°; 110°)

the orbit e , pericentral distance of the orbit p , mass galaxies ratio μ and disk orientation for both galaxies (i, ω) with respect the orbital plane.

TABLE 2
INITIAL POSITION AND VELOCITY.

Coordinates	Gal ₁	Gal ₂
(x, y, z) [kpc]	(-25, 0, 0)	(25, 0, 0)
(v_x, v_y, v_z) [km/s]	(25, 4.1, 0.0)	(-25, -4.1, 0.0)

The orbital plane has been rotated 45° in the polar direction and 45° in the azimuthal direction. Those data are in the reference frame of the simulated box.

2.2. Gas physics

The simulation was performed with the cosmological N-body hydrodynamical code RAMSES (Teyssier 2002). The code uses adaptive mesh refinement, and solves the Euler equations with a second-order Godunov method and MUSCL scheme using a MinMod total variation diminishing scheme to reconstruct the cell centered values at cell interfaces.

The galaxies were set inside a computational box of $L_{\text{box}} = 400$ kpc. The coarse level of the simulation corresponds to $\ell_{\text{min}} = 7$ and $\Delta x_{\text{coarse}} = 3.125$ kpc. We allowed 10 levels of refinement to get a maximum resolution at $\ell_{\text{max}} = 17$ of $\Delta x_{\text{min}} = 3.05$ pc. The refinement is allowed inside a cell if i) its total mass is more than 8 times that of the initial mass resolution, and ii) the Jeans length is resolved by less than 4 cells (Truelove et al. 1997). If we take into account grid regions where number density is above 0.01 cm^{-3} , the worst cell refinement we find is at level 12 with $\Delta x \approx 97$ pc, and cells at refinement level 14 and 15 account for almost $\sim 60\%$ of the total number of cells throughout such areas. Above these, at level 16 we account for the $\sim 16\%$ of cells and at level 17 we account for $\sim 8\%$.

Our simulation includes optically thin (no self-shielding) gas cooling following the Sutherland & Dopita

TABLE 3
INITIAL ISOLATED GALAXY SETUP.

Gaseous disc (Exponential profile)	
Mass [$10^9 M_\odot$]	1.0
Characteristic radius [kpc]	1.0
Truncation radius [kpc]	5.0
Stellar disk (Myamoto-Nagai profile)	
Mass [$10^9 M_\odot$]	2.975
Number of particles	11900000
Characteristic radius [kpc]	0.677
Truncation radius [kpc]	5.0
Stellar bulge (Einasto profile)	
Mass [$10^9 M_\odot$]	0.975
Number of particles	390000
Characteristic radius [kpc]	0.6
Truncation radius [kpc]	1.0
Dark matter halo (NFW profile)	
Mass [$10^9 M_\odot$]	20
Number of particles	200000
Concentration parameter	10
Truncation radius [kpc]	60

(1993) model down to temperature $T = 10^4$ K with a contribution from metals, assuming a primordial composition of the various heavy elements. Below this temperature, the gas can cool down to $T = 10$ K due to metal line cooling (Dalgarno & MacCray 1972).

We adopted a star formation number density threshold of $n_0 = 250 \text{ H cm}^{-3}$ with a star formation efficiency $\epsilon_\star = 0.03$ (e.g. Rasera & Teyssier 2006; Dubois & Teyssier 2008). When a cell reaches the conditions for star formation, stellar (population) particles can be spawned following a Poisson distribution with a mass resolution of $m_{\star, \text{res}} \approx 2 \times 10^2 M_\odot$. In order to ensure numerical stability we do not allow cells to convert more than 50% of the gas into stars within a single time step.

After 10 Myr the most massive stars explode as SN releasing a specific energy of $E_{\text{SN}} = 10^{51}$ erg/ $10 M_\odot$, returning 20 per cent of the stellar particle mass back into the gas with a yield (fraction of metals) of 0.1 inside a sphere of $r_{\text{SN}} = 2\Delta x_{\text{min}}$. In order to capture the delay of stellar feedback energy release from non-thermal processes, we used the delayed cooling implementation of SNe feedback (Teyssier et al. 2013). In this work we use $t_{\text{diss}} \approx 0.25$ Myr and the energy threshold e_{NT} is the one associated to a turbulent velocity dispersion $\sigma_{\text{NT}} \approx 50$ km/s, consistent with our resolution (see Dubois et al. 2015; Prieto & Escala 2016, for details).

In order to follow the evolution of the central BH in the galaxies, we used sink particles (Bleuler & Teyssier 2014). We computed the mass accretion rate onto the BH using the standard Bondi-Hoyle (Bondi 1952) model, \dot{M}_{Bondi} . In such accretion implementation the gas density is computed as an average weighted value taken from the sink's cloud particles using a kernel following Krumholz et al. (2004) as presented in Dubois et al. (2012). Throughout the simulation we cap the accretion rate at the Eddington rate. The initial BH mass for both galaxies is $M_{\text{BH}} = 10^6 M_\odot$, approximately lying on the $M_{\text{BH}} - \sigma_\star$

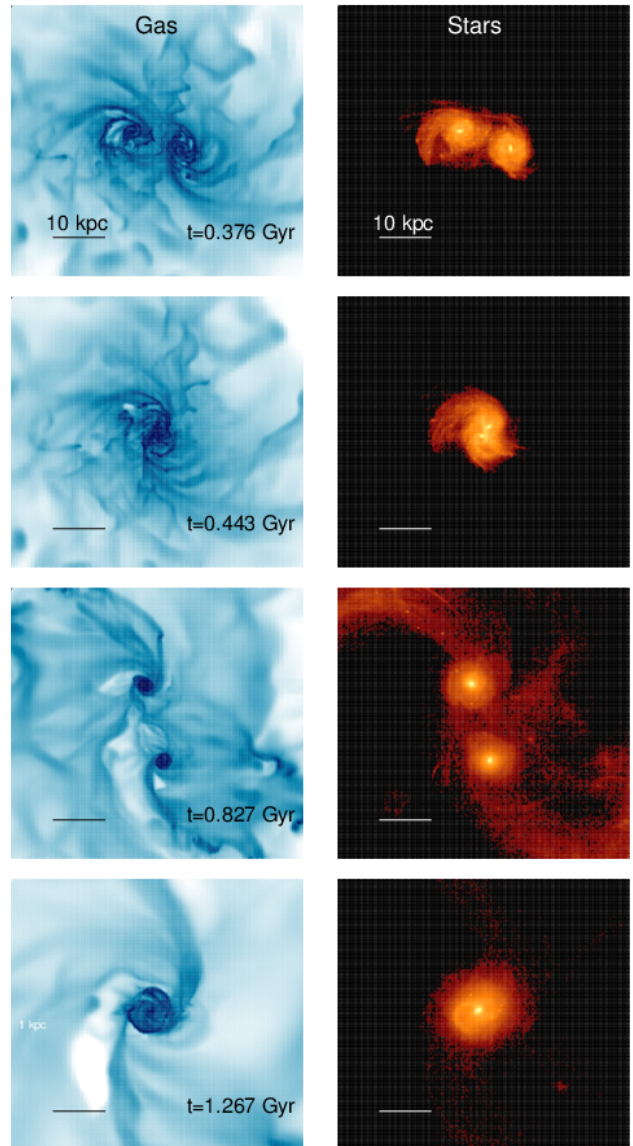


FIG. 1.— Gas number density projection (left column) and stellar mass projection (right column) at different times. From top to bottom: central BHs are at 10 kpc, the first apocenter and the point of coalescence

relation. Assuming a sound speed of $c_s \approx 10 - 30$ km/s (for a gas temperature $T_{\text{gas}} \approx 10^4 - 10^5$ K, note that most of the time the gas is at 10^4 K, the 10^5 K are associated to AGN activity when the gas is expelled from the BH vicinity), the BH influence radius at the beginning of the simulation is $R_{\text{BH}} = G M_{\text{BH}} / c_s^2 \approx 420 - 42 \text{ pc} \approx 140 - 14 \Delta x_{\text{min}}$. In other words, we can resolve the BH influence radius with several cells (note that such radius increases throughout the simulation). In addition to the aforementioned grid refinement criteria, we impose that a 20-sided cubic volume surrounding sink particles, stays fixed at maximum spatial resolution, helping to resolve the BH influence radius and to account for any potential non trivial physical processes occurring nearby. Finally, the BHs particles merge if their separation is lower than $d_{\text{merge}} = 2\Delta x_{\text{min}}$ and if they are gravitationally bound.

We have also included AGN feedback from the central

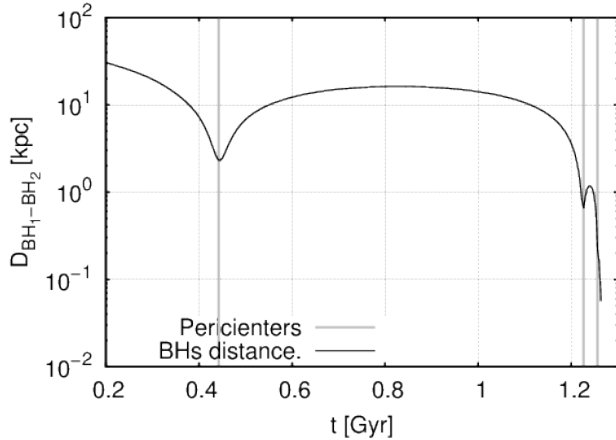


FIG. 2.— BH particles distance as a function of time. The different gray vertical lines mark the first, second and third pericenter passes of the orbit (from left to right). After the third pericenter the BHs approach each other until they finally merge at $t_{\text{merger}} = 1.25$ Gyr, ~ 800 Myr after the first pericenter pass.

BHs. AGN feedback is modeled with thermal energy input (Teyssier et al. 2011; Dubois et al. 2012). The rate of energy deposited by the BH inside the injection radius $r_{\text{inj}} \equiv 4\Delta x_{\text{min}}$ is

$$\dot{E}_{\text{AGN}} = \epsilon_c \epsilon_r \dot{M}_{\text{BH}} c^2. \quad (1)$$

In the above expression, $\epsilon_r = 0.1$ is the radiative efficiency for a standard thin accretion disc (Shakura & Sunyaev 1973) and $\epsilon_c = 0.15$ is the fraction of this energy coupled to the gas in order to reproduce the local BH-galaxy mass relation (Dubois et al. 2012). As explained in Booth & Schaye (2009), in order to avoid gas over-cooling the AGN energy is not released instantaneously every time step Δt but it is accumulated until the surrounding gas temperature can be increased by $\Delta T_{\text{min}} = 10^7$ K. In order to reduce the heating effect of the AGN we have included an extra multiplicative factor of 0.1 to \dot{E}_{AGN} , which is done as otherwise the feedback is too effective at preventing accretion onto the central BHs, and is consistent with the scaling of radiative efficiency and BH mass found in Davis & Laor (2011). Such factor can be interpreted as a lower radiative efficiency, a lower energy coupling or a combination of both effects. This lowering of factor feedback is consistent with how NGC 2623’s energetics are dominated by star formation over AGN feedback Privon et al. (2013).

3. RESULTS

Figure 1 shows four different snapshots throughout the merger, namely (from top to bottom) when the BHs are at a distance of 10 kpc, the first pericenter, the first apocenter and time where systems coalesce (marked by the time in which the SMBHs merge). After the first pericenter pass the system develops two prominent tidal tails producing a “double-tailed” object, which can be appreciated in how the system looks like, at the point of its first apocenter in figure 1.

Before we show results related with SF properties, BH growth and gas dynamics throughout the merger, it is illustrative to look at the BH separation evolution shown

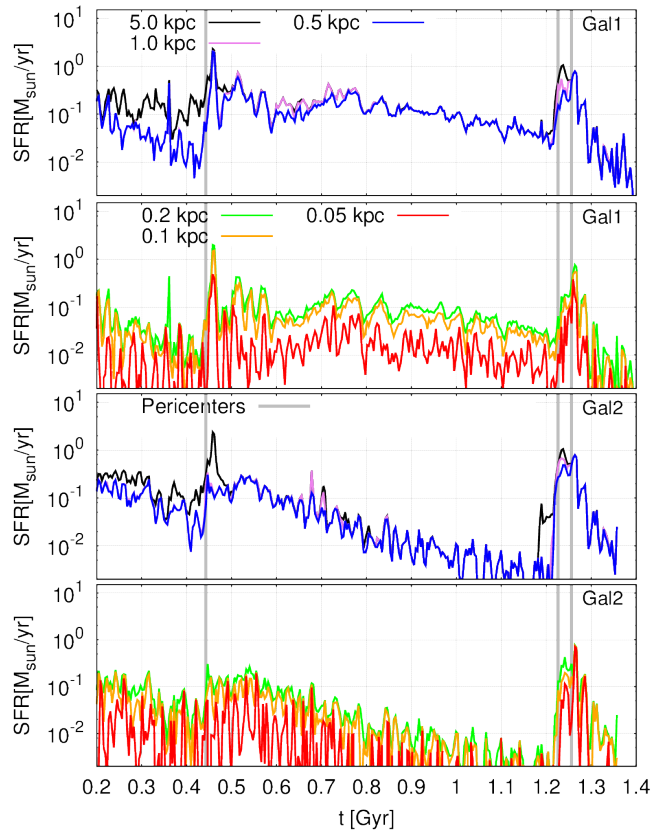


FIG. 3.— Enclosed SFR at different distances from BH particle for both galaxies as a function of time: Inside 5 kpc in black, 1 kpc in violet, 0.5 kpc in blue, 0.2 kpc in green, 0.1 kpc in orange and 0.05 kpc in red. The gray solid vertical lines mark the pericenters of the orbit. It is clear that after each pericenter pass there is a SF burst. Both the second and the third pericenter passes trigger nuclear SF on scales below few 100 pc whereas the first one produces more extended SF at \sim kpc scales.

in figure 2. This quantity is a good proxy for the galactic center separation. The figure shows the time for pericenter passes (in solid gray vertical lines). After the third pericenter the BHs start to orbit around each other, rapidly decreasing their separation until they merge at $t_{\text{merger}} = 1.275$ Gyr. This time corresponds to ~ 800 Myr after the first pericenter. Furthermore, the simulated time of the BH merger depends on the minimum separation adopted (which in our case is able to resolve the sphere influence of the BHs) for the BH coalescence; if the minimum separation is further decreased the BHs will spend more time orbiting each other. The pericenter passes marked by vertical lines in the figure 2 will guide our discussion in the following lines.

3.1. Star formation rate

A number of works have shown how galactic mergers-interactions trigger bursts of SF (e.g. Barnes & Hernquist 1991; Cox et al. 2006; Di Matteo et al. 2007; Hopkins et al. 2008; Moreno et al. 2019). The SF in mergers is not restricted to the galactic nuclear regions (the inner \sim kpc) but it can also be triggered in gaseous tails of the system (e.g. Soifer et al. 1984; Keel et al. 1985; Lawrence et al. 1989). In this analysis we will focus on the nuclear (not tail) SF burst produced by enhancement of gas density due the galactic interactions and we will not

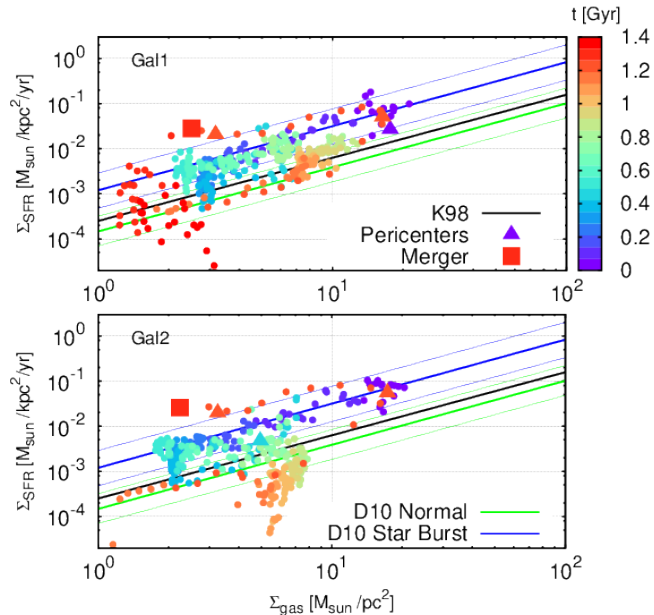


FIG. 4.— Kennicutt-Schmidt relation for both galaxies in small circles. The different colors mark different times. In black solid line the Kennicutt (1998) relation, in green solid line the Daddi et al. (2010) relation for normal galaxies and in blue solid line the Daddi et al. (2010) relation for star bursts. The thin lines mark the error of the corresponding relation.

study the extended, in-tail SF (e.g. Barnes 2004; Chien & Barnes 2010; Renaud et al. 2014).

Figure 3 shows the enclosed SFR inside a given radius of both galaxies throughout the evolution. The SFR is computed as the ratio between the total stellar mass produced in the last ~ 3.75 Myr and a characteristic time defined as the mass weighted stellar age:

$$t_{\star, \text{avg}} = \frac{1}{\sum_i m_{\star, i}} \sum_i t_{\star, i} m_{\star, i}. \quad (2)$$

Then,

$$\text{SFR} = \frac{1}{t_{\star, \text{avg}}} \sum_i m_{\star, i}, \quad (3)$$

where $m_{\star, i}$ and $t_{\star, i}$ are the new stellar population mass and its age, respectively. We computed the SFR inside a sphere centered at the BH position for different radius, namely $R_{\text{SFR}} = 5, 1, 0.5, 0.2, 0.1, 0.05$ kpc.

The SFR in figure 3 shows intermittent behavior due to both stellar and BH feedback. Before any pericenter passages between the galaxies, at scales of \sim few kiloparsec, formation rates generally fluctuate around $\sim 0.1 M_{\odot}/\text{yr}$. We see SF episodes lasting $\sim 30 - 40$ Myr after the pericenter passes. These relatively short periods are explained by the response of the medium to feedback from the massive stellar particles. We also note that star formation evolves differently for both galaxies after their first encounter. At ~ 70 Myr before the first pericenter pass (376 Myr after the start of the simulation, see the first image of figure 1) the spiral arms of the galaxies start to collide (at this time galactic center distance is 10 kpc). This working interface progressively increases the gas density, translating to a burst of SF.

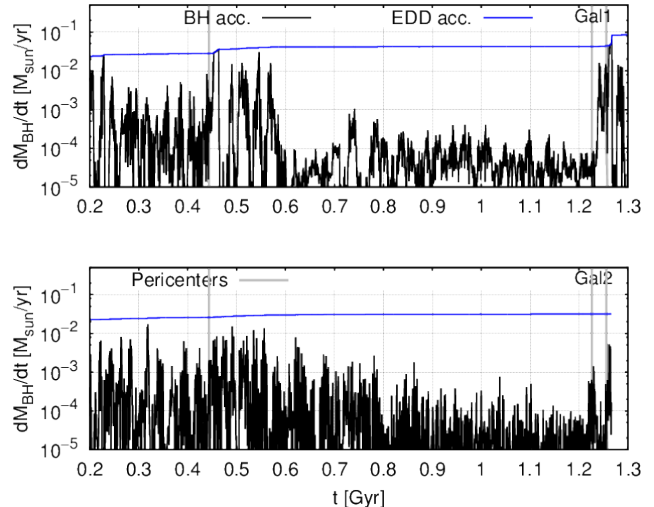


FIG. 5.— Mass accretion rate onto the BHs in black solid line. The solid vertical gray lines mark the pericenters of the orbit. The Eddington mass accretion rate limit is in blue solid line. Both the second and the third pericenter produce a clear increase in the BHAR.

Once the galaxies reach the first pericenter a clear SF burst appears across all distance scales in Galaxy 1, with the SFR reaching \sim few M_{\odot}/yr at distances over 0.1 kpc, showing an enhancement of formation rates exceeding two orders of magnitude, which stems from the nuclear regions of the system. This strong burst lasts around $\gtrsim 30$ Myr (longer for bigger scales), after which the system is left with a relatively high but slowly decreasing nuclear SFR. In the case of Galaxy 2 there is a not too drastic increase in nuclear star formation at 0.1 – 0.2 kpc after the first passage, but like for the first system, there is also a delayed strong SF episode in the outer region of the galaxy, which is itself a response to the galactic arms colliding. The collision of the spiral arms evolves more slowly than the central region collisions, which explains why the high SFRs at large scales are more persistent than the nuclear ones at this stage. After this first passage we see a steady decline in star formation for galaxy 2 (at least until another close passage happens).

The second and third pericenter encounters show prominent increases in the SF activity in both galaxies, where a clear increase is seen on all galactic scales. The second encounter shows a bigger SF enhancement on extended scales at first and then delayed at a close third pericenter passage, star formation from the nuclear regions becomes a highly prominent feature. These high star formation rates are maintained for around 50 – 100 Myr, after which, the central black holes are merged, and while the system starts stabilizing, star formation declines.

These results show a clear correlation between pericenter passes and increases in SF. The SF bursts are localized to different galactic regions depending on the stage of the merger: the first passage trigger extended (above \sim kpc, due to spiral arms collision) SF whereas the second and third pericenter produce new stars at the nuclear region (inside ~ 0.5 kpc).

The SFR values reached in the simulation at the pericenter are in the range of $1 - 10 M_{\odot}/\text{yr}$, below the SFRs measured by Evans et al. (2008) corresponding to

$\sim 50 - 90 M_{\odot}/\text{yr}$, and also below the $\sim 70 M_{\odot}/\text{yr}$ found by Howell et al. (2010) for a system with similar initial conditions as ours (NGC 2623). The simulated values are closer to the $8 M_{\odot}/\text{yr}$ rate found for the system's recent past in Cortijo-Ferrero et al. (2017). This SFRs values are realistic for a merger system (Pearson et al. 2019), albeit it would put our simulation below typical starburst galaxy rates.

Figure 4 shows the Kennicutt-Schmidt relation (Schmidt 1959; Kennicutt 1998, here after K98) for both galaxies as a function of time. In order to compute the galactic disc surface density Σ_{gas} and the surface SFR Σ_{SFR} we have defined a radius R_{disc} and a height h_{disc} inside a box with 12 kpc of side centered at the BH position; the SFR is computed within this cylinder. The equatorial plane of the cylinder is constructed with a point and a normal vector, namely the BH position and the gas angular momentum vector computed inside 2 kpc from the BH position (see appendix A for a discussion about rotational center). Inside the 12 kpc side box we compute the enclosed mass in both the positive and the negative \hat{z} direction as a function of height z . The disc height h_{disc} corresponds to the altitude z where the cylinder contains 90% of the baryonic mass. Following an analogous method we computed the radius R_{disc} as the radius where for a cylinder height h_{disc} the disc contains 90% of the baryonic mass. After this procedure we define

$$\Sigma_{\text{gas}} = \frac{M_{\text{gas}}}{\pi R_{\text{disc}}^2}, \quad (4)$$

where M_{gas} is the gas mass inside the cylinder and

$$\Sigma_{\text{SFR}} = \frac{\text{SFR}}{\pi R_{\text{disc}}^2}, \quad (5)$$

with the SFR computed each ~ 3.75 Myr.

Both systems start near the Daddi et al. (2010) (hereafter D10) Star Burst SF relation and evolves between this and the usual K98 relation (blue-cyan dots) showing no clear transition behaviour around the first merger passage. After around ~ 600 Myr (green to orange transition) where we found a steady decline in SFRs at figure 3, the galaxy 2 system starts going below both the K98 and D10 relations, exhibiting how star formation is not able to keep up with the amount of gas stripped from the galaxy by the merger interaction. Later pericenter passages bring both galaxies above the star burst D10 relation, and after the violent episodes of both SF and AGN feedback that the systems are subjected to, the eventually merged galaxy evolves progressively to the region below the D10 normal galaxies, showing a clear decrease in SFR (see Renaud et al. 2014).

3.2. Black hole evolution

Observational evidence suggests that galactic encounters can trigger AGN activity (e.g. Veilleux et al. 2002; Giavalisco et al. 2004; Treister et al. 2012). In order to feed the BHs the galactic gas should reach the sphere of influence of the central massive objects. To accrete on to the BH, gas orbiting around the BH must lose angular momentum, resulting in an inward gas mass flow in the galaxy. This can be triggered by gravitational torques acting on the gas due to the galaxy-galaxy interaction (e.g. Barnes 1988; Barnes & Hernquist 1991;

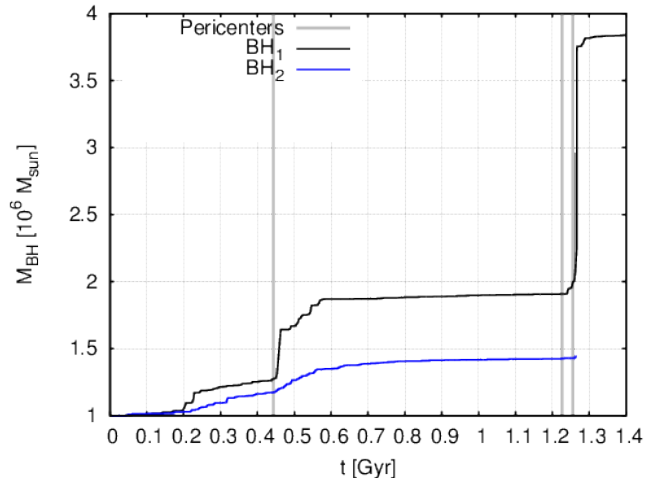


FIG. 6.— BH mass evolution. In solid black line the BH mass associated to galaxy 1 and in solid blue line the BH mass associated to galaxy 2. The solid vertical gray lines mark the pericenters of the orbit.

Di Matteo et al. 2005; Cox et al. 2008) or in general by any type of torque (gravitational, pressure gradients/ hydrodynamic, magnetic, or viscous) capable of changing the angular momentum of the gaseous component of the galaxy.

Figure 5 shows the BH mass accretion rate as a function of time for both galaxies. The black hole accretion rates (BHAR) oscillate in the range of $\sim 10^{-2} - 10^{-4} M_{\odot}/\text{yr}$ over the first ~ 600 Myr, where we see galaxy 1 approaching (and eventually peaking at) the Eddington limit on different occasions. After the first pericenter passage, AGN feedback strongly regulates accretion rates, lowering them for at least an order of magnitude.

Following the low BHAR after the first pericenter passage, in the two following passes, both systems exhibit clear peaks due to the funnelling of gas towards the central galaxy regions. These peaks are more pronounced on galaxy 1 than in galaxy 2, the first reaching BHAR values of a few $10^{-2} M_{\odot}/\text{yr}$, whilst the second only has low (albeit pronounced) peaks of a $10^{-3} M_{\odot}/\text{yr}$. After these two last encounters the BHs merge (where just before this, galaxy 1 accreted at the Eddington rate for a short period of time).

Figure 6 shows the BH masses as a function of time. Because the differences in their mass accretion rate the BH masses are also different for both objects. The BH₁ mass shows a clearer increase with the first pericenter compared with BH₂, as can be seen from its mass accretion rate (figure 4). We confirm that after undergoing a strong mass gaining episode, BH₁'s mass stays nearly constant for ~ 600 Myr, with a mass of $\sim 1.8 \times 10^6 M_{\odot}$. During this time interval the galaxies have reached their first pericenter producing an enhancement in the BH₁ mass accretion rate and consequently in its mass. This BH growth is not associated with galactic bulge coalescence and show that BHs can grow in stages before the galactic bulge merge (Medling et al. 2013).

In contrast to the BH₁ evolution, the second compact object does show a clear increase in the first pericenter but it is substantially lower, as can be seen from the low mass accretion rate shown in figure 4 (which caps at

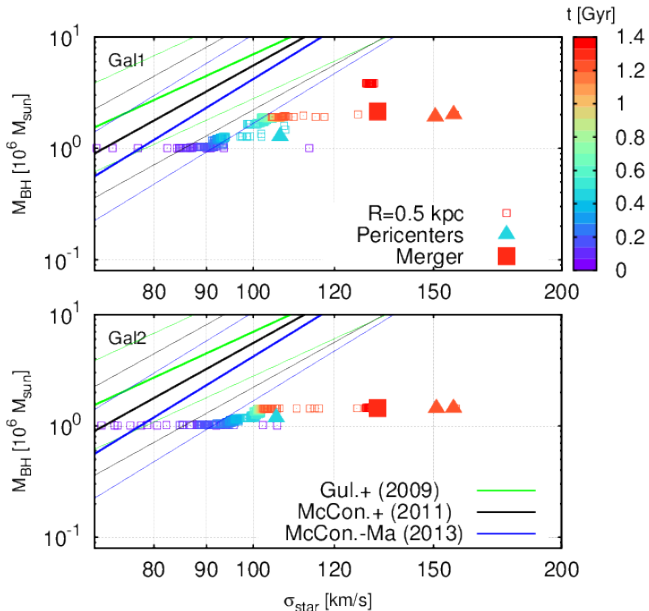


FIG. 7.— BH mass-bulge stellar velocity dispersion relation. Different colors mark different times. Filled circles mark the relation taking into account all stars inside 1 kpc around the central BH and empty squares mark the relation for stars inside 0.5 kpc around the central BH. The broad black solid line shows the McConnell et al. (2011) relation, the broad blue solid line shows the McConnell & Ma (2013) relation and the broad green solid line shows the Gültekin et al. (2009) relation. The thin green, blue and black line are the corresponding relation 0.4 dex above and below the central one.

$\sim 10^{-2} M_{\odot}/\text{yr}$, which is not necessarily low, but there is a big amount of perceivable variation in rates). The evolution becomes nearly flat, with a low amount of growth until the merger. At the time of coalescence, BH₁ had grown nearly twice as much as what BH₂ had grown through accretion, and after merger, the remnant BH ends up at $\sim 3.8 \times 10^6 M_{\odot}$. This final value would put the final BH mass well below the LIRG galaxy mergers (like NGC 2623) found in the GOALS sample (Haan et al. (2011)), and although initially this is neither an indication that the black holes are not accreting enough gas through the merger evolution, nor that the BH initial masses are wrong, we can further the analysis by checking how the M- σ relation evolves throughout the simulation.

Given the BH mass at each point and the stellar velocities, it is possible to compute the $M_{\text{BH}}-\sigma_{\star}$ (“M-sigma”) relation. (McConnell et al. 2011; McConnell & Ma 2013; Gültekin et al. 2009) Figure 7 shows such relation as a function of time. We have initialized the simulation with a BH mass $M_{\text{BH}} = 10^6 M_{\odot}$ and a bulge velocity dispersion $\sigma_b \approx 110$ km/s, which means our setup is inside the empirical relation of McConnell & Ma (2013) when using the velocity dispersion from the < 0.5 kpc region. Even though it is normal for velocity dispersion to grow quickly in proportion to BH mass in a merger process due to the strong dynamical perturbation the bulges suffer (and therefore we expect a tendency that the measured M- σ values should partially stray to the right of the relation), we see in the figure both galaxies quickly moving far away from the empirical relation. This means

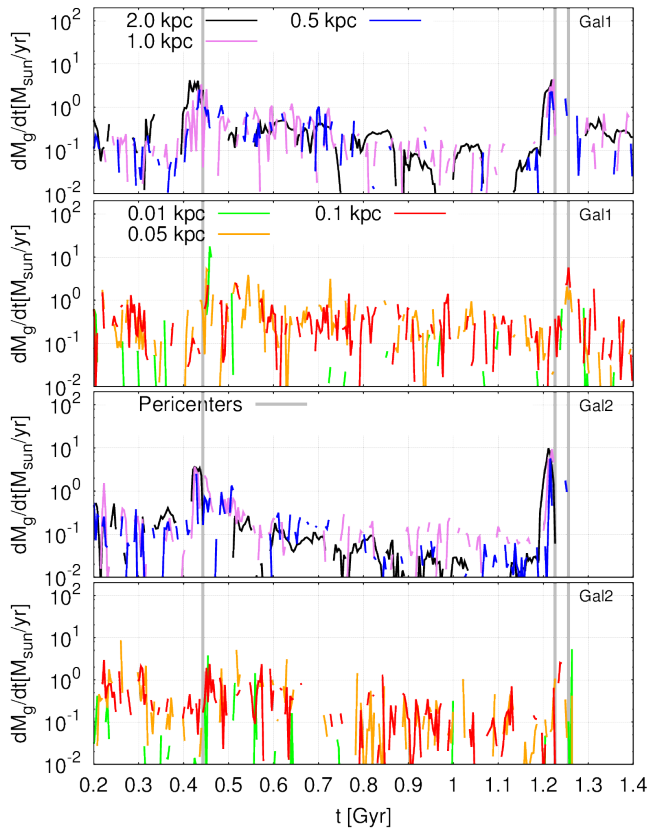


FIG. 8.— Inward gas mass accretion rate as a function of time at different distances from the galactic stellar center of mass: 2 kpc in black, 1 kpc in violet, 0.5 kpc in blue, 0.1 kpc in green, 0.05 kpc in orange and 0.01 kpc in red. The solid vertical gray lines mark the pericenters of the galactic orbit. The figure shows that pericenters correlate with peaks of mass accretion rate.

that the feeding of the BHs is not being able to catch up with the growth of velocity dispersion (it should be noted that after the stellar bulges merge, velocity dispersion should not increase, and BH feeding could slowly bring the system back to the empirical relation as the galaxy stabilizes).

To further support how BHs are growing less than what is expected of them, we see for instance, that BH₁ grows from $10^6 M_{\odot}$ to $\sim 2 \times 10^6 M_{\odot}$ in 1.2 Gyr, and if the Eddington accretion rate is $\dot{M}_{\text{Edd}}(t) = \frac{M_{\text{BH}}(t)}{t_{\text{Sal}}}$ (with the Salpeter timescale being $t_{\text{Sal}} = 4.5$ Myr for our radiative efficiency), we would have an average accretion rate of $\approx 2,5 \times 10^{-3} \dot{M}_{\text{Edd}}$, well under typical feeding expected for radiative AGN feedback to be relevant.

The apparent culprit of these overall lower than expected average BHAR, would be the amount of thermal feedback being put back into the grid, which heats the gas surrounding the vicinity of our BHs too effectively for accretion to be steadily maintained. This is further evidenced by how even though torques at the hill radius are sustained all through the simulation (see section 3.4), this does not translate into a feeding of the black holes, as we see instead that the only important feeding episodes occur in the initial stages of the simulation and at close passages (where material is too efficiently transported towards the center, allowing gas dynamics to overcome the heating effect of feedback).

The straightforward AGN feedback approach that we are using from Dubois et al. (2012) was developed for cosmological simulations, and even though it has seen successful use in that context, the main difference here is that at the high resolutions we achieve, such simple recipe may result in the failure to capture the correct small scale physics that model the heating of the central bulges by the BHs. It has been shown that different methods for dealing with BH feedback may yield quite different results, and that direct injection of thermal energy to galactic cores may produce strong and persistent outflows or cavities in central regions that suppress accretion (Wurster & Thacker 2013). It is then imperative that we try to capture the more detailed heating structure that is produced by the radiative transfer of the soft X-ray photons that produce quasar-mode feedback. There have been successful efforts at capturing the heating rate from the expected X-ray emission of the central AGN from Choi et al. (2012), but this recipe is still at its heart a direct injection of energy back to the galactic core, and does not offer any accounting of radiative transfer effects.

A more consistent option for improving our feedback recipe, would be to include radiation coupling to our hydrodynamics through RAMSES-RT, in the code presented by Rosdahl et al. (2013) and Rosdahl & Teyssier (2015). Quasar feedback has already been modelled in this way (Bieri et al. 2017), and it relies in the coupling of hydrodynamics with the radiative transfer of photons being introduced by the sink particle into the grid through an AGN template spectral distribution, allowing for a detailed accounting of the production and reprocessing of X-ray radiation (and therefore the overall heating mechanisms) produced by the innermost regions. The introduction of the RT module would also allow for a more consistent modelling of SN feedback, and presents the opportunity for future work.

3.3. Gas accretion rate

In the last section we showed that peaks of BH mass accretion rate correlate with the pericentric passages, suggesting a connection between close encounters and enhancement of gas inflows in galaxies. Under this scenario it is useful to look at the inward gas mass accretion rate at different radii. Figure 8 shows the inward gas mass accretion rate at different distances from the stellar center of mass. As with the KS computation, we have constructed a disc perpendicular to the gas angular momentum vector. After that, in order to compute the gas accretion rate we look for the stellar center of mass inside 2 kpc around the BH for each galaxy. Given the position \vec{r}_{CM} and bulk velocity \vec{v}_{CM} of the center of mass we have computed the inflowing gas mass accretion rate as

$$\dot{M}_{\text{g}} = \sum_i \rho_i (\vec{v}_i - \vec{v}_{\text{CM}}) \cdot \Delta \vec{A}_i. \quad (6)$$

where \vec{v}_i is the gas cell velocity and \vec{A}_i is the surface element crossed by the gas in a direction parallel to the radial vector $\vec{r}_i - \vec{r}_{\text{CM}}$, with \vec{r}_i the gas cell position. The sum is computed inside an annulus of width Δx_{min} for $r \leq 200$ pc, corresponding to the level of refinement 17 and $32 \Delta x_{\text{min}}$ for $r \geq 500$ pc, corresponding to the refinement level 12.

Figure 8 shows a clear correlation between peaks of gas mass accretion rate on scales $\gtrsim 0.5$ kpc and close passes for both galaxies (first and third panel from top). The first pericenter pass is associated with a gas mass accretion rate as high as $\sim 5 M_{\odot}/\text{yr}$. A few Myr before the second pericenter pass mass accretion rates reach \sim few $5 - 10 M_{\odot}/\text{yr}$ at large scales. Such episodes of inflowing mass on large scales are consistent with enhancement of SF in pericenters as shown in figure 3. The causal relation between these two phenomena can be seen by comparing the SFR and the mass accretion rate: the close passes produce mass inflows which are followed after a few Myr by bursts of SF.

At small scales (below ~ 100 pc), the enhancement in mass accretion rate at the first pericenter is not as significant as it is in large scales, except for very short bursts of inflow at $0.05 - 0.01$ kpc scales in Galaxy 1. The inflowing mass accretion rate reaches values that are above $\sim 10 M_{\odot}/\text{yr}$ in galaxy 1 in the nucleus at 10 pc in this brief burst (which happens at distances below the order of the BH sphere of influence), but rates are generally around the $\sim 1 M_{\odot}/\text{yr}$ value, and are sustained in a somewhat irregular fashion before the first encounter. Galaxy 2 shows a slightly more consistent mass accretion rate in the same period of time at similar scales, but rates are not perceivably higher. The second and third pericenter passes show an enhancement in mass accretion at small scales. the amount of inflowing mass is able to trigger (after few Myr) SF bursts and feed the BHs as has been shown in the previous sections. In particular, at the third pericenter pass the gas inflow rate approaches $\sim 10 M_{\odot}/\text{yr}$ due to the gas bulges coalescence.

We conclude that there is a correlation between peaks of gas mass accretion rate, SFR, and BHAR associated with pericenter passages. In other words, close galactic encounters trigger mass inflows crossing the BH influence radius, producing SF bursts and lighting up AGN activity in galactic centers.

3.4. Torques on the gas

At this point we have shown that throughout the merger process there are episodes of efficient gas inflows toward the galaxy centers. In order to fully understand the origin of mass transport into the galactic center it is necessary to quantify the torques acting on the gas, in order to link mass inflow episodes with angular momentum losses (see appendix C).

Figure 9 shows the torques acting on the galactic disc at different radius as a function of time. Before computing the torques, we have defined the galactic disc in the same way we did it to compute the KS relation and the gas mass transport.

We have computed the torques with respect the stellar center of mass \vec{r}_{CM} as a proxy for the rotational center of each spiral galaxy (see appendix A for a discussion about rotational centers). In order to do that, it is necessary to set a non-rotating coordinate system free falling with the stars. In such a frame, the acceleration of a particle becomes $\vec{a}'_i = \vec{a}_i - \vec{a}_{\text{CM}}$, where \vec{a}_i is the particle acceleration with respect an inertial reference frame (the center of the fixed simulation box in our case) and \vec{a}_{CM} is the acceleration of the stellar center of mass with respect the same inertial frame (see appendix B). Then, in the co-moving

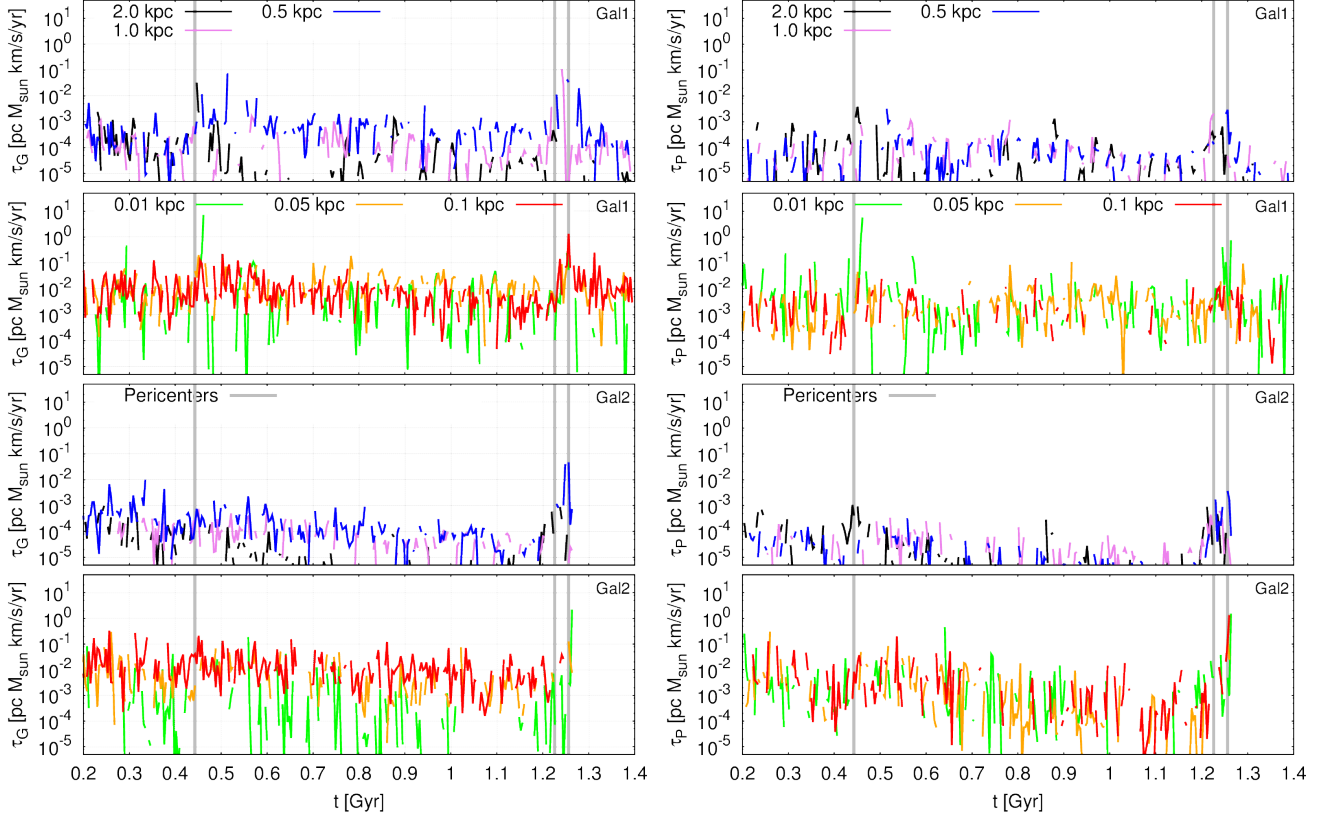


FIG. 9.— Left: Total gravitational torque on the gas associated to inward mass transport at different distances from the stellar center of mass: 2 kpc in black, 1 kpc in violet, 0.5 kpc in blue, 0.1 kpc in red, 0.05 kpc in orange and 0.01 kpc in green. The solid vertical gray lines mark the pericenters of the orbit. Right: Same as left column but for the hydrodynamic torque. The figure shows that pericenters are associated with increases in torques.

reference frame the torques can be computed as

$$\vec{\tau}^i = \sum_i m_i (\vec{r}_i - \vec{r}_{\text{CM}}) \times (\vec{a}_i - \vec{a}_{\text{CM}}). \quad (7)$$

In the previous expression \vec{r}_i is the cell position, m_i is the gas cell mass. The acceleration \vec{a}_i is the combination of the gravitational acceleration $-\nabla\phi_i$ and the acceleration associated to hydrodynamic on the gas $\nabla P_i/\rho_i$, where ϕ_i is the gravitational potential at a given cell and P_i is the pressure in the same cell.

Because the galactic disc is defined in terms of the disc angular momentum, negative torques imply a loss of angular momentum and a resulting inward mass transport. Figure 9 shows $-\vec{\tau}^i$, i.e. torques producing net inward mass transport inside an annulus at a given distance from the galactic centers (the regions without data are dominated by outward mass transport torques). The sum is computed inside an annulus of width Δx_{min} for $r \leq 200$ pc and $32 \Delta x_{\text{min}}$ for $r \geq 500$ pc, as in the gas mass accretion rate computation.

The left column of figure 9 shows that at large scales ($\gtrsim 0.5$ kpc) both galaxies show large fluctuations in gravitational torques with galaxy 1 reaching larger torque values with higher fluctuation. In both galaxies gravitational torques are more important at 0.5 kpc than at larger radii. It can be understood in terms of the higher gas concentration at lower galactic radii.

The huge fluctuations in gravitational torques at large scales makes difficult to identify a peak associated with

the first pericenter in both galaxies. In galaxy 1 it is possible to identify a coherent increase at 2 kpc about \sim few Myr after the first passage. On the other hand, in galaxy 2 no gravitational torque peak can be identified at large scales.

In galaxy 2 the late pericenter passages are associated with increased gravitational torques on larger scales (mainly at 0.5 kpc scales for the second passage). In galaxy 1 it is more difficult to recognize a torque increase (only having measured one relevant torque spike at 1 kpc between passages). We also see some torque presence at 0.5 kpc after the merger of the systems.

Gravitational torques acting on the galactic central region, i.e. less than 100 pc from the stellar center of mass, show a clear enhancement associated with the second and third pericenter passes but an almost imperceptible change during the first pericenter pass for both galaxies. Figure 9 shows that the inner galactic region, besides a very short increase of torque at 10 pc in galaxy 1 after the first passage, feels the maximum gravitational torque around the third pericenter pass (with a very big spike at the smallest scales for galaxy 2 when the systems are about to merge). Such strong torques acting on the galactic gas produces gas inflows and feeds the central massive objects, lighting up the AGN. It is also of note, that gravitational torques feature most importantly, at 100 pc scales, which aligns with how the BH influence sphere helps with gas transport at this distance.

The right column of figure 9 shows the hydrodynamic

torques associated with inward mass transport. At large spatial scales hydrodynamic torques are lower and more sporadic than gravitational torques. This hydrodynamical torque values become closer to gravitational ones at pericenter passages, where especially for galaxy 2, we see features at every passage.

Within the galactic nuclei the hydrodynamic torques match quite well with gravitational torques at the smallest scales, showing peaks in the same places where their counterparts do. Such enhancements are at the same level as the gravitational torques showing that both mechanisms are working to redistribute matter in the later stages of the merger. In other words, hydrodynamic torques work in tandem with gravitational torque in order to redistribute mass and angular momentum in the galactic disc.

4. DISCUSSION AND CONCLUSIONS

With the aim of studying the connection between torques and mass transport in galactic discs, we have simulated a galaxy merger employing realistic initial conditions based in Privon et al. (2013). The SFR reaches values of $\sim 1 - 10 M_{\odot}/\text{yr}$, below the observational measurements from (Evans et al. 2008; Howell et al. 2010) for NGC 2623 specifically, but closer to the values presented in Cortijo-Ferrero et al. (2017), this puts our system below the star forming capabilities of a starbursting system, but inside expected rates for generic merger systems (Pearson et al. 2019). The final BH mass of the system is $M_{\text{BH}} \approx 3.8 \times 10^6 M_{\odot}$, around one or two order of magnitudes below the usual values presented in Haan et al. (2011) and below the dispersion of the ‘‘M-sigma’’ relation (Gültekin et al. 2009). This low BH mass is due to low amounts of accretion stemming from the effectiveness feedback has at heating the immediate environment around our sink particles, calling for an improvement of the feedback model at our resolution, one option being the inclusion of a fully coupled radiation hydrodynamical feedback (see Bieri et al. (2017)).

Our results confirm that galactic encounters can trigger bursts of SF (e.g. Barnes & Hernquist 1991; Mihos & Hernquist 1996; Springel et al. 2005; Gabor et al. 2016). The first pericenter pass clearly increase the SF of both galaxies but those increases are more evident beyond ~ 500 pc from the galactic center, when it reaches \sim few M_{\odot}/yr . At these higher scales the SFR enhancement is due to the gas density increase triggered by the collision of the gaseous galactic spiral arms. Because the first pericenter pass has a nuclear separation of ~ 2 kpc, most of the SF is localized at those distances from the center. In contrast, the second and third pericenter passes trigger bursts of SF at the inner hundred of parsecs, again reaching \sim few M_{\odot}/yr . At this stage the gas density has increased due to mass transport, resulting in a prominent nuclear SF burst.

Besides the SFR, the BHAR peaks also show correlations with pericenter encounters. Whereas one of the BHs has a growth rate correlated with its three pericenter passes the other one correlates better with its second and third pericenter passes. In both cases it is evident that the second and third pericenter passes increase the

BHAR, reaching values of $\sim 50 - 100\%$ and $\sim 25\%$ of the corresponding Eddington limits for the BHs (corresponding to a few $\sim 10^{-2} M_{\odot}/\text{yr}$ and a few $\sim 10^{-3} M_{\odot}/\text{yr}$). Such high mass accretion rate onto the compact objects will trigger the AGN activity.

Both phenomena described above, i.e., star formation activity and BH accretion, are driven by the amount of gas available to form stars and to feed the BHs. Our simulation shows that pericenter passes correlate with peaks of gas mass accretion rates driving gas mass density variations in the BH vicinity, i.e. inside its influence radius. The first encounter produces a direct mass inflow of $\sim 3 M_{\odot}/\text{yr}$ outside of ~ 500 pc, associated with the galaxy-galaxy crossing. This encounter triggers \sim kpc scale SF in both galaxies. On the other hand, at smaller scales ($r \lesssim 100$ pc) the first pericenter produces a big increase in the mass accretion rate for one of the galaxies (reaching a short peak of $\sim 10 M_{\odot}/\text{yr}$), and a smaller increase for the second one, but still enough to produce SF and to feed one of the BHs. The second and third pericenter passes produce a clear enhancement in mass accretion rate onto the nuclear galactic region. In fact, at the third closest passage the gas mass inflow at inner scales is simultaneously high for both systems and as such, the galactic gas entering the BH sphere of influence efficiently feeds the BHs and triggers nuclear SF bursts.

Neglecting magnetic fields and viscosity, any variation on the gas angular momentum will be due to torques from both gravitational and pressure gradient forces (see appendix C). In other words, the merger triggers changes in the gas angular momentum due to variations in the gravitational potential and gas pressure. The former are produced due to the dynamics of the merger which is characterized by strong gravitational interactions, and the latter is produced by gas layers with strong differences in density and/or temperature. Such conditions naturally arise when both galaxies cross each other and finally merge. We have shown that pericenter passes correlate with both gravitational and hydrodynamic torque peaks. In general, gravitational torques dominate over hydrodynamic torques but at inner scales pressure gradient torques can reach values approaching that of the gravitational ones helping to radially transport gas in galactic disc. These torques redistribute angular momentum allowing inward mass transport onto the galactic center. The high resolution of our simulation showed that such gas inflows can cross the BH influence radius producing peaks in the BHAR and triggering SF burst.

ACKNOWLEDGEMENTS

Powered@NLHPC: This research was partially supported by the supercomputing infrastructure of the NLHPC (ECM-02). The Geryon cluster at the Centro de AstroIngenieria UC was extensively used for the analysis calculations performed in this paper. JP is funded by ESO-Chile Comite Mixto grant ORP 79/16. AE acknowledges partial support from the Center for Astrophysics and Associated Technologies CATA (PFB06) and Proyecto Regular Fondecyt (grant 1181663). G.C.P. acknowledges support from the University of Florida.

REFERENCES

Angulo, R. E., Springel, V., White, S. D. M., Jenkins, A., Baugh, C. M., & Frenk, C. S. 2012, MNRAS, 426, 2046

Armus, L., et al. 2009, PASP, 121, 559

- Bahcall J. N., Kirhakos S. & Schneider D. P., 1995, *ApJ*, 447, L1
- Barnes J. E., 1988, *ApJ*, 331, 699
- Barnes J. E., 2004, *MNRAS*, 350, 798
- Barnes J. E., & Hernquist L. E. 1991, *ApJ*, 370, L65
- Bieri, R., Dubois, Y., Rosdahl, J., et al. 2017, *MNRAS*, 464, 1854
- Bleuler A. & Teyssier R., 2014, *MNRAS*, 445, 4015
- Blumenthal K. A., Barnes J. E., 2018, *MNRAS*, 479, 3952
- Bondi H., 1952, *MNRAS*, 112, 195
- Booth C. M. & Schaye J., 2009, *MNRAS*, 398, 53
- Bouché N., Dekel A., Genzel R., Genel S., Cresci G., Förster Schreiber N. M., Shapiro K. L., Davies R. I., Tacconi L. Bussmann, R. S., et al. 2012, *ApJ*, 744, 150
- Chien L.-H., & Barnes J. E., 2010, *MNRAS*, 407, 43
- Choi E., Ostriker J. P., Naab T., Johansson P. H., 2012, *ApJ*, 754, 125
- Cortijo-Ferrero C., 2017, *A&A*, 607, 70
- Cox T. J., Jonsson P., Primack J. R., & Somerville R. S., 2006, *MNRAS*, 373, 1013
- Cox T. J., Jonsson P., Somerville R. S., Primack J. R. & Dekel A., 2008, *MNRAS*, 384, 386
- Daddi E., Elbaz D., Walter F., Bournaud F., Salmi F., Carilli C., Dannerbauer H., Dickinson M., Monaco P. & Riechers D., 2010, *ApJ*, 714, 118
- Dalgarno, A. & McCray, R. A., 1972, *ARA&A*, 10, 375
- Debuhr J., Quataert E., Ma Ch.-P., *MNRAS*, 412, 1341
- Di Matteo T., Springel V. & Hernquist L., 2005, *Nature*, 433, 604
- Di Matteo P., Combes F. & Melchior A. & Semelin B., 2007, *A&A*, 468, 61
- Dubois Y. & Teyssier R., 2008, *A&A*, 477, 79
- Dubois, Y., Devriendt, J., Slyz, A., & Teyssier, R. 2012, *MNRAS*, 420, 2662
- Dubois Y., et al. 2014, *MNRAS*, 444, 1453
- Dubois Y., Volonteri M., Silk J., Devriendt J., Slyz A. & Teyssier R., 2015, *MNRAS*, 452, 1502
- Duc P. A., Brinks E., Wink J. E., & Mirabel I. F., 1997, *A&A*, 326, 537
- Engel, H., et al. 2010, *ApJ*, 724, 233
- Evans A. S., et al. 2008, *ApJ*, 675, L69
- Gabor J. M., Capelo P. R., Volonteri M., Bournaud F., Bellovary J., Governato F. & Quinn T., 2016, *A&A*, 592, 62
- Genel Sh., Vogelsberger M., Springel V., Sijacki D., Nelson D., Snyder G., Rodriguez-Gomez V., Torrey P. & Hernquist L., *MNRAS*, 2014, 445, 175
- Giavalisco, M., Ferguson, H. C., Koekemoer, A. M., et al. 2004, *ApJ*, 600, L93
- Gültekin K., Richstone D. O., Gebhardt K., Lauer T.R., Tremaine S., Aller M. C., Bender R., Dressler A., Faber S. M., Filippenko A. V., Green R., Ho L. C., Kormendy J., Magorrian J., Pinkney J. & Siopis C., 2009, *ApJ*, 698, 198
- Haan S., et al., 2011, *AJ*, 141, 100
- Hahn, O., Teyssier, R., & Carollo, C. M. 2010, *MNRAS*, 405, 274
- Hopkins Ph. F., Hernquist L., Cox T. J., Kereš, Dušan, 2008, *ApJS*, 175, 356, 2015, *MNRAS*, 450, 53
- Hopkins, Ph. F., 2015, *MNRAS*, 450, 53
- Howell J. H., et al. 2010, *ApJ*, 715, 572
- Jogee S., et al. 2009, *ApJ*, 697, 1971
- Keel W. C., Kennicutt R. C., Jr. Hummel, E. & van der Hulst J. M. 1985, *AJ*, 90, 708
- Kennicutt R. C. Jr., 1998, *ApJ*, 498, 541
- Krumholz M. R., MaKee C. F. & Klein R. I., 2004, *ApJ*, 611, 399
- Larson K. L., Sanders D. B., Barnes J. E., Ishida C. M., Evans A. S., Mazzarella J. M., Kim D. C., Privon G. C., Mirabel I. F. & Flewelling H. A. Lawrence A., Rowan-Robinson M., Leech K., Jones D. H. P. & Wall J. V., 1989, *MNRAS*, 240, 329
- Maiolino R., Comastri A., Gilli R., et al. 2003, *MNRAS*, 344, L59
- Mayer L., Kazantzidis S., Escala A. & Callegari S., *Nature*, 466, 1082
- McConnell N. J., Ma Ch., Gebhardt K., Wright Sh. A., Murphy J. D., Lauer T. R., Graham J. R. & Richstone D. O., 2011, *Nature*, 480, 215
- McConnell N. J. & Ma Ch.-P., 2013, *ApJ*, 764, 184
- Medling A. et al., 2015, *ApJ*, 803, 61
- Mihos, J. C. & Hernquist, L. 1996, *ApJ*, 464, 641
- Moreno J., et al., 2019, *MNRAS*, 485, 1320
- Navarro J. F., Frenk C. S., White S. D. M., 1996, *ApJ*, 462, 563
- Newton, R. D. A., & Kay, S. T. 2013, *MNRAS*, 434, 3606
- Pearson W. J., et al., 2019b, *A&A*, 631, A51
- Perret V., Renaud F., Epinat B., Amram P., Bournaud F., Contini T., Teyssier R. & Lambert J.-C., 2014, *A&A*, 562A, 1
- Petric, A. O., et al. 2011, *ApJ*, 730, 28
- Powell L. C., Bournaud F., Chapon D. & Teyssier R., 2013, *MNRAS*, 434, 1028
- Prieto J. & Escala A. (PE16), 2016, *MNRAS*, 460, 4018
- Privon G. C., Barnes J. E., Evans A. S., Hibbard J. E., Yun M. S., Mazzarella J. M., Armus, L. & Surace, J., 2013, *ApJ*, 771, 120
- Sanders D.B. & Mirabel I.F., 1996, *ARA&A* 34, 749
- Renaud F., Bournaud F., Kraljic K. & Duc P.-A., 2014, *MNRAS*, 442, 33
- Rasera Y. & Teyssier R., 2006, *A&A*, 445, 1
- Rosdahl J., Teyssier R., 2015, *MNRAS*, 449, 4380
- Rosdahl J., Blaizot J., Aubert D., Stranex T., Teyssier R., 2013, *MNRAS*, 436, 2188
- Sanders D. B., Soifer B. T., Elias J. H., Madore B. F., Matthews K., Neugebauer G., & Scoville N. Z. 1988, *ApJ*, 325, 74
- Schmidt, M., 1959, *ApJ*, 129, 243
- Schweizer, F. 1982, *ApJ*, 252, 455
- Shakura N. I. & Sunyaev R. A., 1973, *A&A*, 24, 337
- Soifer B. T., et al. 1984, *ApJL*, 278, L71
- Springel, V., Di Matteo, T., & Hernquist, L. 2005, *MNRAS*, 361, 776
- Stierwalt et al., 2013, *ApJS*, 206, 1
- Sutherland R. S. & Dopita M. A., 1993, *ApJ Sup.*, 88, 253
- Teyssier R., 2002, *A&A*, 385, 337
- Teyssier R., Chapon D. & Bournaud F., 2010, *ApJ*, 720, L149
- Teyssier R., Moore B., Martizzi D., Dubois Y. & Mayer L., 2011, *MNRAS*, 414, 195
- Teyssier R., Pontzen A., Dubois Y. & Read J. I., 2013, *MNRAS*, 429, 3068
- Toomre, A., & Toomre, J. 1972, *ApJ*, 178, 623
- Treister E., Schawinski K., Urry C. M. & Simmons B. D., 2012, *ApJ*, 758, L39
- Truelove J. K., Klein R. I., McKee Ch. F., Holliman J. H., Howell L. H. & Greenough J. A., 1997, *ApJL*, 489, 179
- U V., et al. 2012, *ApJS*, 203, 9
- Veilleux S., Kim D.-C., & Sanders D. B., 2002, *ApJS*, 143, 315
- Wadsley, J. W., Veeravalli, G., & Couchman, H. M. P. 2008, *MNRAS*, 387, 427
- Davis, S.W. & Laor A., 2011, *ApJ* 728 98
- Wurster, J. & Thacker, R. J., 2013, *MNRAS*, 431, 539

A. APPENDIX: ROTATION CENTER

The rotational center of a system composed by particles of mass m_i at position \vec{r}_i and acceleration \vec{a}_i , and where the amount of particles well-represent the phase space near such center, can be defined as the point \vec{r}_{rot} where the torque

$$\vec{\tau}_{\text{rot}} = \sum_i m_i (\vec{r}_i - \vec{r}_{\text{rot}}) \times (\vec{a}_i - \vec{a}_{\text{rot}}) \quad (8)$$

inside a given volume is null, with \vec{a}_{rot} the rotational center acceleration. In a well approximated system which is supported by ideal rotation, all the accelerations will point to a common center, the rotational center, then the cross product position-acceleration will be null. In systems with a given degree of turbulence and strong noise in its acceleration field, such null point does not necessarily exist, here the task reduces to searching for minima in the torque field to define our rotational center, which necessarily introduces degeneracy in its estimation.

A kinematic approach to identify the rotational center of a system can be based in the previous dynamical definition. In this case, instead of focusing on the particle accelerations it is useful to look at the particle velocities \vec{v}_i . Then the rotational center will be the point where the angular momentum

$$\vec{L}_{\text{rot}} = \sum_i m_i (\vec{r}_i - \vec{r}_{\text{rot}}) \times (\vec{v}_i - \vec{v}_{\text{rot}}) \quad (9)$$

inside a given volume is maximized. Here \vec{v}_{rot} is the velocity of the rotational center. Note that in this case the cross product position-velocity should be a maximum. As with the dynamical definition, if the system has a given degree of turbulence, it would be possible to find more than one center of rotation. We note that if our context was understood as a generic dynamical system, our search criterion reduces to finding the best candidate fulfilling the characteristics of a non-stationary irrational vortex, where \vec{L}_{rot} is the local circulation field maxima.

The process of identifying a rotational center is computationally expensive as it requires computing the angular momentum (or torque) inside a given volume for each point in the space. Given the 3D map for the modulus of the angular momentum it is necessary to look for peaks in the angular momentum distribution. In other words it is necessary to look for ‘‘clumps’’ of angular momentum. Given the ‘‘clumps’’ of angular momentum it is possible to compute the centroid of such objects to define rotational centers. Thus, identifying the stellar center of mass given an ansatz for the rotational center (the BH positions for instance) is faster, computationally.

B. APPENDIX: NON-INERTIAL FRAMES

Inside an accelerating reference frame the Newtonian dynamical equations are modified. In such moving frame an observer will describe the movement of any object as influenced by ‘‘fictitious forces’’. Quantitatively, from a moving system with position \vec{R} with respect an inertial reference frame the force described by an observer at \vec{R} acting on a particle at position \vec{r}_i is

$$m_i \frac{d^2 \vec{r}'_i}{dt^2} = \vec{F}_i - m_i \frac{d^2 \vec{R}}{dt^2} - m_i \vec{\omega} \times (\vec{\omega} \times \vec{r}'_i) - 2m_i \vec{\omega} \times \vec{v}'_i - m_i \frac{d\vec{\omega}}{dt}, \quad (10)$$

where m_i is the mass particle $\vec{r}'_i = \vec{r}_i - \vec{R}$ is the particle position with respect the moving system position \vec{R} and \vec{r}_i the particle position with respect an inertial reference frame. \vec{F}_i is the net force acting on the particle i (due to the magnetic, gravitational, viscous or hydrodynamic contribution), $\vec{\omega}$ is the angular velocity of the moving system and $\vec{v}'_i = d\vec{r}'_i/dt$.

In the simple case when $\vec{\omega} = \vec{0}$, i.e. a moving reference frame without rotation, with \vec{a}'_i the particle acceleration with respect the moving system, \vec{a}_i the particle acceleration with respect an inertial frame and \vec{A} the moving system acceleration with respect the same inertial reference frame it is possible to write

$$\vec{a}'_i = \vec{a}_i - \vec{A}, \quad (11)$$

C. APPENDIX: TORQUES-MASS TRANSPORT RELATION

The momentum conservation equation in its conservative form in Cartesian coordinates x_i can be written as

$$\frac{\partial(\rho v_k)}{\partial t} + \frac{\partial}{\partial x_i} (R_{kl} + P_{kl} + B_{kl} - G_{kl} - S_{kl}) = 0, \quad (12)$$

where ρ is the gas mass density and v_i is the Cartesian component of the gas velocity. R_{kl} , P_{kl} , B_{kl} , G_{kl} and S_{kl} are the hydrodynamical stress, the pressure stress, the magnetic stress, the gravitational stress and the viscous stress, respectively. The stresses are defined by:

$$R_{kl} = \rho v_k v_l, \quad (13)$$

$$P_{kl} = \delta_{kl} P, \quad (14)$$

$$B_{kl} = \frac{1}{4\pi} \left(B_k B_l - \frac{1}{2} B^2 \delta_{kl} \right) \quad (15)$$

$$G_{kl} = \frac{1}{4\pi G} \left[\frac{\partial \phi}{\partial x_k} \frac{\partial \phi}{\partial x_l} - \frac{1}{2} (\nabla \phi)^2 \delta_{kl} \right], \quad (16)$$

$$S_{kl} = \rho \nu \left(\frac{\partial v_k}{\partial x_l} + \frac{\partial v_l}{\partial x_k} - \frac{2}{3} \delta_{kl} \nabla \cdot \vec{v} \right), \quad (17)$$

where P is the gas pressure, B_k the cartesian component of the magnetic field, B the modulus of the magnetic field, ϕ the gravitational potential, ν is the kinematic viscosity and δ_{kl} is the Kronecker delta symbol.

Neglecting the magnetic term and the dissipative-viscous term (Balbus 2003) the momentum conservation equation can be written as

$$\frac{\partial}{\partial t} (\rho v_k) + \frac{\partial}{\partial x_l} (\rho v_k v_l) + \frac{\partial P}{\partial x_k} - \rho \frac{\partial \phi}{\partial x_k} = 0, \quad (18)$$

and taking the cross product between the Cartesian position \vec{x} and eq. 18 (applying $\epsilon_{ijk} x_j$, with ϵ_{ijk} the Levi-Civita symbol) it is possible to derive the angular momentum conservation equation and after some algebra it is possible to write the \hat{z} component of this equation as

$$\frac{\partial}{\partial t} (\rho \ell_z) = - [\ell_z \rho \nabla \cdot \vec{v} + \vec{v} \cdot \nabla (\rho \ell_z) + \tau_z^P + \tau_z^G], \quad (19)$$

from where it is possible to get the gas mass density variation

$$\frac{\partial \rho}{\partial t} = -\frac{1}{\ell_z} \left[\rho \frac{\partial \ell_z}{\partial t} + \ell_z \rho \nabla \cdot \vec{v} + \vec{v} \cdot \nabla (\rho \ell_z) + \tau_z^P + \tau_z^G \right], \quad (20)$$

where $\ell_z = (\vec{x} \times \vec{v}) \cdot \hat{z}$ is the z component of the gas specific angular momentum, $\tau_z^G = \rho (\vec{x} \times \nabla \phi) \cdot \hat{z}$ is the z component of the gravitational torque and $\tau_z^P = (\vec{x} \times \nabla P) \cdot \hat{z}$ is the z component of the hydrodynamic torque.

Equation 20 relates the changes in gas density ρ with torques $\tau_z^{P,G}$ acting on the gas. For a system starting from an axisymmetric stationary state with $\vec{v} = v(r) \hat{\theta}$ and $\rho = \rho(r)$ the azimuthal perturbations in both gas pressure and gravitational potential are the sources of changes in gas density, i.e. both hydrodynamic torques and gravitational torques are able to transport matter from a given radius to another radius of the system.